Chemical Physics 559 (2022) 111558

Contents lists available at ScienceDirect

Chemical Physics

journal homepage: www.elsevier.com/locate/chemphys

Direct Z-scheme heterojunction rutile-TiO_2/g-C_3N_4 catalyst constructed by solid grinding method for photocatalysis degradation

Genxiang Li [a], Yandi Cai [c], Xiudie Wang [a], Lei Zhang [a,b,*], Qiao Xie [a], Peng Chen [a], Chuanjiang Li [a], Jingfang Sun [c,*], Tingzhen Li [a,b,*], Lin Dong [c]

[a] School of Environmental and Chemical Engineering, Chongqing Three Gorges University, Chongqing 404000, PR China
[b] Key Laboratory of Water Environment Evolution and Pollution Control in the Three Gorges Reservoir, Chongqing Three Gorges University, Chongqing 404000, PR China
[c] Jiangsu Key Laboratory of Vehicle Emissions Control, Center of Modern Analysis, School of Environment, Nanjing University, Nanjing 210093, PR China

ARTICLE INFO

Keywords:
direct Z-scheme heterojunction
rutile-TiO_2/g-C_3N_4
Solid grinding method
Photocatalytic performance

ABSTRACT

Constructing a direct Z-scheme heterojunction is an effective method to improve the catalytic performance of photocatalyst. Here, the direct Z-scheme heterojunction rutile-TiO_2/g-C_3N_4 photocatalyst was constructed by a simple solid grinding method. This method can not only avoid the weak activity of rutile-TiO_2 in high synthesized temperature condition, but also precisely control the amount of g-C_3N_4. The evaluation of photodegradation reaction suggests that the rutile-TiO_2/g-C_3N_4 photocatalyst exhibits higher photodegradation efficiency than the pure rutile-TiO_2 and the pure g-C_3N_4 under simulated sunlight irradiation, and the optimal photocatalytic performance is achieved when the mass ratio of rutile-TiO_2 to g-C_3N_4 is 2:5. The experimental results prove that a direct Z-scheme heterojunction is formed over the rutile-TiO_2/g-C_3N_4 photocatalyst, which promotes the effective electron-hole separation and the higher redox potential over the rutile-TiO_2/g-C_3N_4 photocatalyst. This work provides an attractive strategy to construct the direct Z-scheme photocatalyst consisted of rutile-TiO_2 and g-C_3N_4.

1. Introduction

Semiconductor photocatalysis is a green technology, which has played a very noteworthy role in the fields of global energy storage and environmental remediation [1,2]. Since the first report on water splitting of graphitic carbon nitride (g-C_3N_4) under visible light irradiation was published in 2009, g-C_3N_4 has been widely acknowledged as photocatalyst due to its exceptional visible light response, high reduction ability and physicochemical stability [3–7]. However, the photocatalytic performance of pure g-C_3N_4 is limited by the weak oxidative ability of holes and fast recombination rate of photogenerated charge carriers [8–11]. Therefore, it's highly desirable to explore a reasonable approach to overcome these drawbacks.

To date, researchers have made great efforts to enhance the charge separation of g-C_3N_4, including metals or non-metals doping [12,13] and heterojunction construction [14]. In order to increase the response range of visible light, it is necessary to reduce the band gap of semiconductor photocatalyst, however, it is thermodynamically disadvantageous to the photocatalytic redox reaction due to the positive shift of conduction band and/or the negative shift of valence band, thus the both aspects are contradictory [15]. Among these methods, heterojunction construction via coupling with other semiconductors can solve the above contradiction and has attracted considerable interests [16,17]. Especially, a direct Z-scheme heterojunction displays outstanding photocatalytic performance owing to its high redox potential and effective spatial separation of carriers without electron transfer mediator [18]. It has been reported that the modification of TiO_2 to form heterojunction can improve the photocatalytic performance of g-C_3N_4 by suppressing the recombination of photogenerated carriers [19,20]. For instance, Hao et al. synthesized rutile TiO_2@g-C_3N_4 core–shell nanorod arrays, which shows an enhanced photocatalytic activity for the photodegradation of RhB dye [21]. Xia et al. reported TiO_2@g-C_3N_4 core–shell heterojunction photocatalysts with uniform mesoporous structures, such an extraordinary core–shell heterojunction significantly inhibited the recombination of photogenerated electrons and holes for better visible light photocatalytic performance [22]. Additionally, TiO_2/

* Corresponding authors at: School of Environmental and Chemical Engineering, Chongqing Three Gorges University, Chongqing 404000, PR China (L. Zhang and T. Li).
E-mail addresses: leizhang@sanxiau.edu.cn (L. Zhang), sunjf@nju.edu.cn (J. Sun), litingzhen@163.com (T. Li).

https://doi.org/10.1016/j.chemphys.2022.111558
Received 17 December 2021; Received in revised form 15 February 2022; Accepted 18 April 2022
Available online 20 April 2022

g-C_3N_4 heterojunctions were typically prepared by high-temperature calcination of the physical mixtures of g-C_3N_4 precursors and TiO_2 (or their precursors) [23–25]. It is worth noting that, for TiO_2/g-C_3N_4 composites, after calcination at high temperature, TiO_2 is easy to agglomerate to deactivate and the amount of g-C_3N_4 is difficult to precisely control. Thus, the search for a simple and effective synthesis method to solve the problems and make TiO_2/g-C_3N_4 heterojunction with high photocatalytic activity is necessary.

In this work, a direct Z-scheme heterojunction rutile-TiO_2/g-C_3N_4 catalyst was successfully constructed. The rutile-TiO_2 was prepared by hydrolysis of $TiCl_4$ in pure water at 60 ℃, and it is found that the photocatalytic activity of the prepared rutile-TiO_2/g-C_3N_4 samples obviously decreases with increasing the calcination temperature, and therefore the high temperature calcination process is not conducive for rutile-TiO_2/g-C_3N_4. To the best of our knowledge, the solid grinding method can resolve the aforementioned problems in the synthesis of rutile-TiO_2/g-C_3N_4 heterojunction photocatalyst. Thus, a series of rutile-TiO_2/g-C_3N_4 photocatalysts were prepared by solid grinding method. The obtained photocatalysts were characterized by X-ray diffraction (XRD), Fourier transform-infrared spectroscopy (FTIR), X-ray photoelectron spectroscopy (XPS), High-resolution transmission electron microscopy (HRTEM), UV–visible diffused reflectance spectroscopy (UV–Vis DRS) and photoelectrochemical tests. We focus on studying the structure and photocatalytic performance of rutile-TiO_2/g-C_3N_4 photocatalyst, and the reaction mechanism of photocatalytic degradation over the rutile-TiO_2/g-C_3N_4 photocatalyst.

2. Experimental section

2.1. Materials

Titanium tetrachloride ($TiCl_4$) was purchased from Shanghai Chemical Reagent Company, China. Melamine ($C_3H_6N_6$) was purchased from Sigma Aldrich. Ethylenediamine tetraacetic acid disodium (EDTA-2Na) was purchased from Xilong Scientific Co., Ltd. Isopropyl alcohol (IPA) and p-benzoquinone (p-BQ) were purchased from Cheng Du Chron Chemicals Co., Ltd. These chemicals were of analytical grade and used without further purification. Deionized water was used in all experiments.

2.2. Preparation of photocatalysts

2.2.1. Preparation of g-C_3N_4 nanosheet (CN)

10 g of melamine was added to an alumina crucible with a cover and calcined in a muffle furnace at 550 ℃ for 3 h using a ramping rate of 10 ℃/min. The yellow bulk g-C_3N_4 was obtained and ground into the powder. The final product of g-C_3N_4 nanosheet was prepared by thermal exfoliation of the above bulk g-C_3N_4. In brief, 1 g of bulk g-C_3N_4 powder was placed into an alumina crucible without cover and calcined under the same thermal conditions as the above bulk g-C_3N_4. After air-cooling to room temperature, the CN nanosheet sample was obtained.

2.2.2. Preparation of rutile-TiO_2 (RT)

2 mL $TiCl_4$ was slowly dripped into 20 mL water under gently magnetic stirring at room temperature. The hydrolysis process was a highly exothermic reaction and released a large quantity of HCl fumes. After continuous stirring, the mixed solutions became a transparent aqueous solution. Then the resulting solution was heated to 60 ℃ in a temperature-controlled water bath and kept for 6 h. After completing the condensation and nucleation process, the precipitate formed in the solutions was aged for several hours, collected by centrifugation (25 min at 9000 rpm) and sonication, washed repeatedly with water to remove Cl^- ions, dried at 80 ℃ overnight in an oven and grinded in an agate mortar with a pestle to obtain the RT sample.

2.2.3. Preparation of rutile-TiO_2/g-C_3N_4

The rutile-TiO_2/g-C_3N_4 samples were prepared by mixing the different ratios of CN nanosheet and RT nanopowder and grinding for 10 min gently to obtain a uniform, smooth powder. The mass ratios of RT to CN are 1:5, 2:5, 1:1 and 5:2.

2.3. Characterization

XRD patterns of samples were obtained in a Philips X'pert Pro diffractometer with Ni-filtered Cu Kα1 radiation ($\lambda = 0.15408$ nm, 40 kV and 40 mA).

FTIR measurements were conducted by a FTIR Prestige-21 spectrophotometer with the reference of KBr. A spectrum was collected from 500 to 2000 cm^{-1} with the spectral resolution of 16 cm^{-1}.

XPS experiments were performed on a PHI 5000 Versa Probe X-ray photoelectron spectrometer, via a monochromatic Al *Kα* (1486.6 kV) radiation source (15 kW), the samples were degassed in a UHV chamber ($<5 \times 10^{-7}$ Pa) at room temperature prior to measurements. The C 1 *s* peak at 284.6 eV was used as a reference for calibrating all binding energies of the samples. And the XPS data was processed by the software of XPSPEAK.

TEM and HRTEM images were taken by JEM-2100 instrument operated at an acceleration voltage of 200 kV.

UV–vis diffuse reflectance spectroscopy (UV–Vis DRS) were recorded in 200–800 nm region by a Shimadzu UV-2401 spectrophotometer using $BaSO_4$ as reference.

Electrochemical measurements of photocatalysts on an electrochemical workstation (VersaSTAT3-400, USA) were conducted in a standard three-electrode system. The photocatalyst powder was deposited on indium-tin oxide (ITO) glass electrode with an active area of ca. 1 cm^2 as the working electrode. The saturated calomel electrode (SCE) and platinum sheet were employed as the reference electrode and counter electrode, respectively. The 0.1 M Na_2SO_4 aqueous solution was served as electrolyte. A 300 W Xe lamp was used as irradiation. The electrochemical impedance spectra (EIS) were tested at 0.5 V on a frequency range from 0.1 Hz to 100000 Hz. The transient photocurrent response measurements were conducted at 0.0 V bias potential (vs SCE) using a 30 s on–off cycle. The Mott-Schottky plots were measured in the dark at a frequency of 2000 Hz with the polarization potential from −1.5 to 1 V (vs SCE).

2.4. Evaluation of photocatalytic activity

The evaluation of the photocatalytic activity of the as-prepared catalysts was carried out in a quartz glass reactor. A 10 mg portion of catalyst was dispersed in 10 mL RhB dye (10 $mg{\cdot}L^{-1}$). A 500 W Xenon lamp equipped with a circulating cooling system of a jacket of flowing water as the light source. During the photodegradation process, 1 mL suspension was withdrawn at the given time internals (25 min) to analyze the concentration of RhB solution by UV–vis spectrophotometer (Shimadzu UV-2450, Japan) at wavelength of 554 nm. The removal rate can be calculated as C_t/C_0, where C_t the concentration of RhB at the given reaction time and C_0 was the initial concentration of RhB after the adsorption equilibrium in the dark room. To investigate the stability of photocatalyst, after the photocatalytic reaction, the photocatalyst was collected and reused in the recycling experiments.

The active component of holes (h^+), superoxide radicals ($^{\bullet}O_2^-$) and hydroxyl radicals ($^{\bullet}OH$) were captured using ethylenediamine tetraacetic acid disodium (EDTA-2Na, 5 $mmol{\cdot}L^{-1}$), p-benzoquinone (p-BQ, 5 $mmol{\cdot}L^{-1}$) and isopropyl alcohol (IPA, 5 $mmol{\cdot}L^{-1}$), respectively. The experimental procedures (using the sunlight as the light source) and the analyzed method were similar to the described above, except the addition of scavengers into the solution to scavenge the active components.

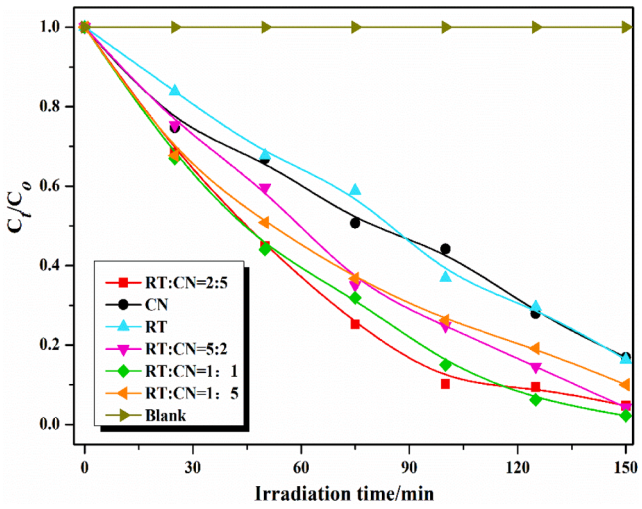

Fig. 1. The photodegradation activity of pure CN, RT and RTCN photocatalysts for RhB under simulated sunlight irradiation.

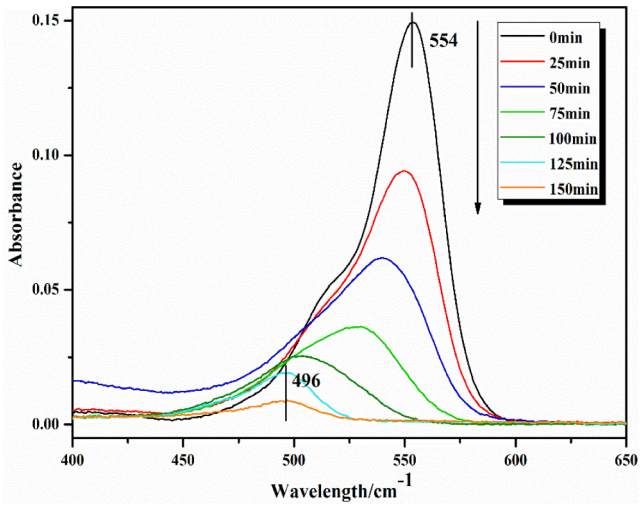

Fig. 3. UV–Vis absorption spectral of reaction solution at different reaction times over the RTCN photocatalyst (monitored by a Shimadzu UV-2450 spectrophotometer).

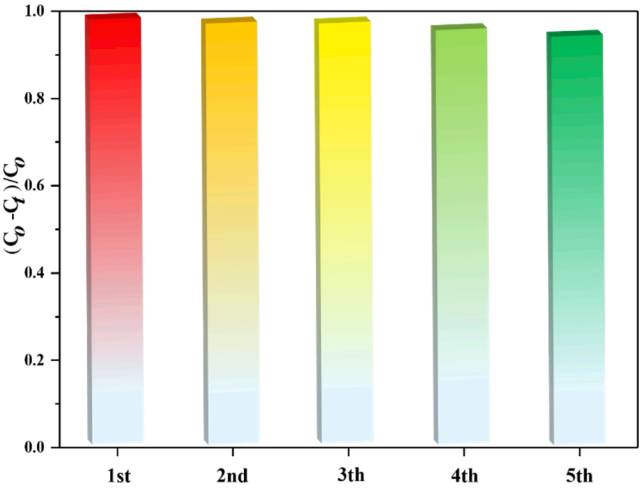

Fig. 2. Stability test for RhB degradation over the RTCN photocatalyst.

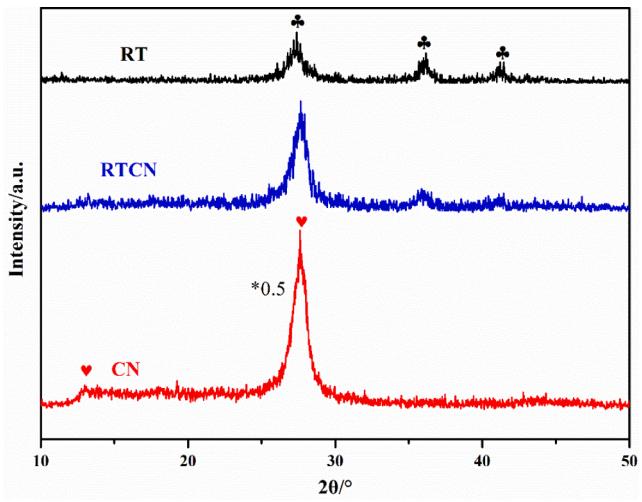

Fig. 4. XRD patterns of the CN, RT and RTCN samples.

3. Results and discussion

3.1. Photocatalytic performance

The photodegradation activity of photocatalysts was tested by degrading RhB under simulated sunlight irradiation. The adsorption–desorption equilibrium of RhB was achieved over the photocatalysts after 50 min in the dark. It can be seen that the concentration of RhB has no apparent decreased without photocatalysts (blank test), indicating that the self-degradation of RhB can be ignored under the present experimental conditions. As we can see from Fig. 1, both pure RT and CN own the low removal efficiency of RhB. Interestingly, after CN is combined with RT to construct rutile-TiO_2/g-C_3N_4 samples, a remarkable enhanced photocatalytic activity obtained. With increasing the mass ratio of RT and CN, the degradation rate of RhB exhibits the feature of rising in the beginning and then declining, and the photocatalytic activity of samples follows the order of RT:CN = 2:5 > RT:CN = 1:1 > RT:CN = 1:5 > RT:CN = 5:2 > CN ≈ RT. In addition, the effect of annealing temperature on the photocatalytic performance of the RT:CN = 2:5 was further tested, as shown in Fig. S1, it can be seen that the catalytic performance of the samples obviously decreases with the increase of annealing temperature, which indicates that the high temperature calcination process is disadvantageous to the catalytic performance of rutile-TiO_2/g-C_3N_4 samples. In order to explore the reasons of improving photocatalytic activity over rutile-TiO_2/g-C_3N_4 photocatalyst, the RT:CN = 2:5 (noted as RTCN in the latter sections) is chosen to further analyze with various characterization techniques.

To evaluate the stability of the RTCN photocatalyst, the RTCN photocatalyst was repeatedly used for five times to test the degradation activity of RhB after 150 min irradiation. As shown in Fig. 2, the photocatalytic activity of the RTCN photocatalyst slightly decrease after five recycles. It can be found that the RTCN photocatalyst itself turns slightly red to indicate the adsorption of RhB molecules over the surface of the RTCN photocatalyst, which can be responsible for the insignificant decline of photocatalytic performance [26]. These results demonstrate that the RTCN photocatalyst possesses excellent stability during the process of photocatalytic RhB degradation.

UV–Vis absorption spectra of reaction solution were collected to analyze the products of degradation process. As shown in Fig. 3, it can be seen that the absorption intensity of RhB obviously decreases and the maximum absorption wavelength shifts from 554 nm to 496 nm with the increase of irradiation time. Watanable and co-workers [27,28] reported that the reason of the hypsochromic shift of the RhB absorption could be ascribed to the *N*-deethylation processes. The characteristic wavelengths of RhB were corresponded to a step-by-step deethylation of RhB to give

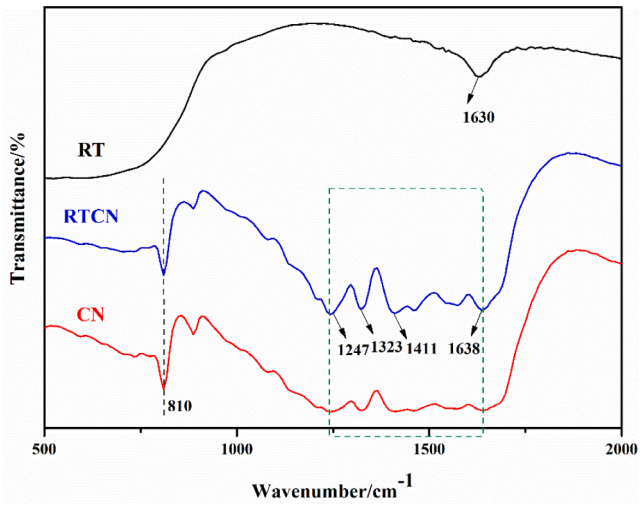

Fig. 5. The FTIR spectra of the as-prepared CN, RT and RTCN samples.

539 nm (*N,N,N'*-ethylated rhodamine, TER), 522 nm (*N,N'*-ethylated rhodamine, DER), 510 nm (*N*-ethylated rhodamine, MER), 498 nm (rhodamine) [29,30]. After 125 min of irradiation time, the maximum absorption wavelength keeps at 496 nm and its intensity gradually weakens with increasing the reaction time, which indicates that rhodamine can be further degraded and possibly mineralized to CO_2 and H_2O.

3.2. Structure and morphology

The crystal structures of the as-prepared pure CN, RT and RTCN samples were characterized by XRD. As shown in Fig. 4 for the pure CN sample, the two typical diffraction peaks of graphitic carbon nitride at around 13.1° and 27.6°, which are indexed to the (1 0 0) crystal plane of tri-s-triazine repeated units and (0 0 2) crystal plane of the stacks of the aromatic segments respectively, are existed [31–33]. For the pure RT sample, the characteristic peaks located at $2\theta = 27.4°$, 36.1°, 41.2° are assigned to the (1 1 0), (1 0 1) and (1 1 1) planes of rutile TiO_2, respectively (JCPDF NO.21–1276). For the RTCN sample, there is no any other new peaks except the diffraction peaks of rutile TiO_2 and g-C_3N_4, which indicates that the RTCN sample is composed of rutile TiO_2 and g-C_3N_4.

The FTIR were utilized to investigate the chemical compositions and bonding structures of the CN, RT and RTCN samples. As shown in Fig. 5, the broad absorption band at 1240–1640 cm^{-1} is resulted from two kinds of chemical bonding of pure CN. The bands at 1247, 1323, and 1411 cm^{-1} are assigned to the sp_3 C—N breathing modes, and the band at 1638 cm^{-1} is ascribed to the aromatic sp_2 C═N stretching vibration [34–36]. The sharp band at 810 cm^{-1} is corresponded to the characteristic bending of tri-s-triazine units [37,38]. As for the pure RT, the broad absorption band between 500 and 800 cm^{-1} is attributed to the vibration modes of Ti—O and Ti—O—Ti [26]. The band centered at 1630 cm^{-1} is related to the adsorbed water molecules on the surface of sample. For the RTCN sample, the main characteristic bands are the same as the pure CN and no band shift can be detected, suggesting that adding rutile TiO_2 by solid grinding has no effect on the chemical bonding of g-C_3N_4 in the RTCN sample, which is consistent with the XRD results.

XPS was conducted to analyze the electronic states and chemical compositions on the surface of the CN, RT and RTCN samples. The XPS results are shown in Fig. 6, and the peaks were fitted by Gaussian-Lorentz curves. For the high-resolution C 1*s* spectrum of the CN sample, two main peaks centered at 284.6 and 287.9 eV can be attributed to the sp_2-bonded carbon atoms of C—C and N—C═N groups, respectively [39]. For the RT sample, two deconvolution peaks at 284.6 and 288.6 eV are all attributable to carbon contamination. In the N 1*s* spectra of the

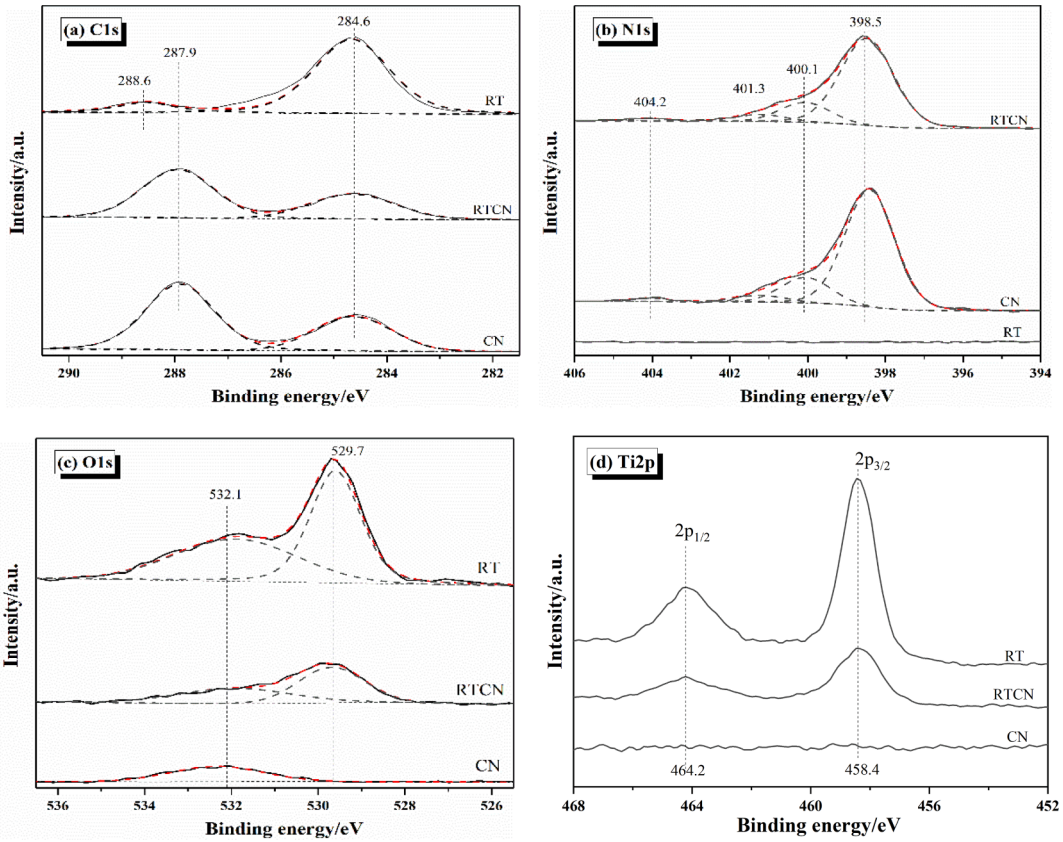

Fig. 6. XPS spectra of (a) C 1s, (b) N 1s, (c) O 1s and (d) Ti 2p of the CN, RT and RTCN samples.

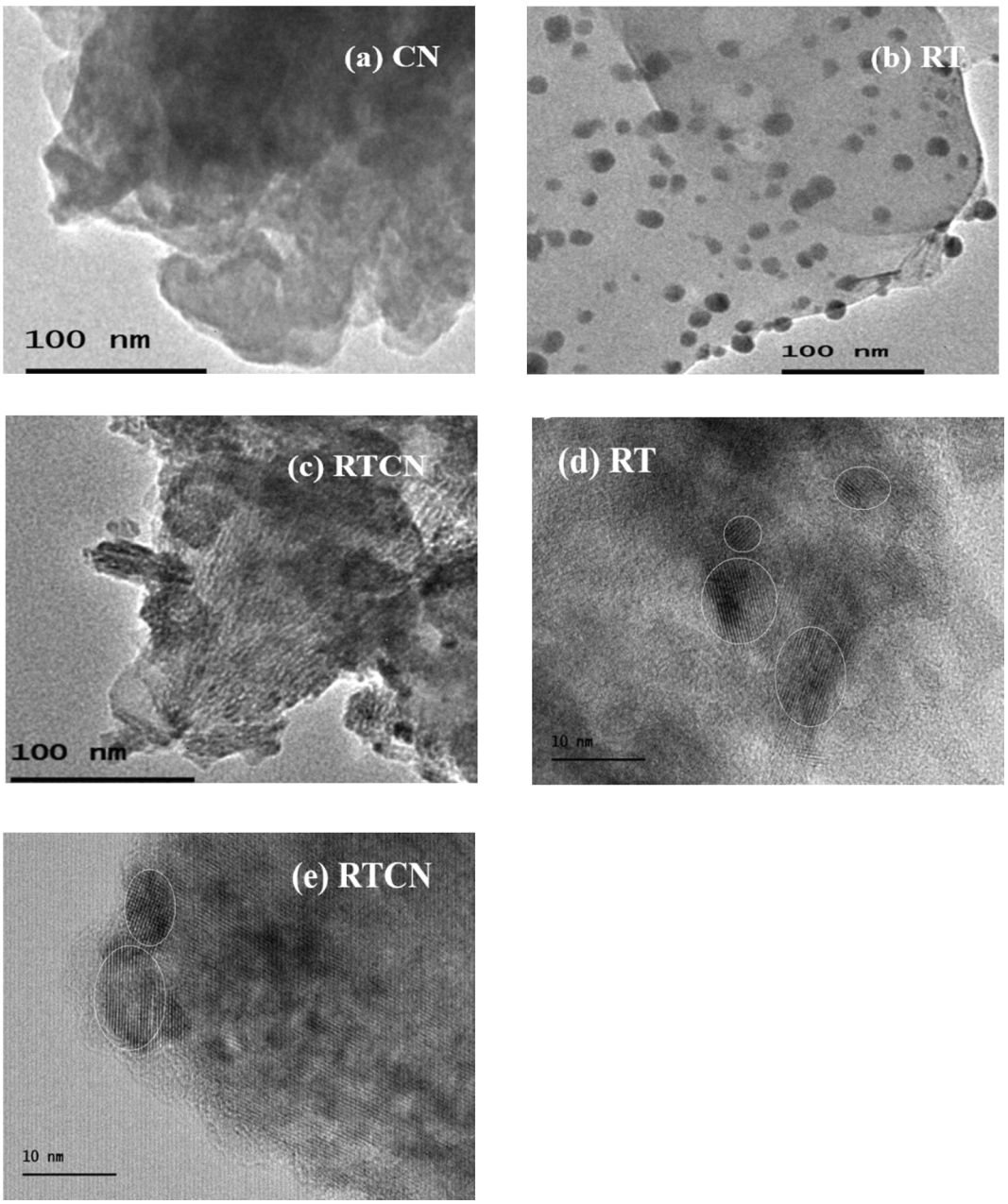

Fig. 7. TEM images of (a) CN, (b) RT, (c) RTCN, and HRTEM images of (d) RT and (e) RTCN composite.

CN sample, four peaks with binding energies at 398.5, 400.1, 401.3 and 404.2 eV can be observed. The main contribution peak at 398.5 eV can be assigned to sp_2 hybridized aromatic N (C═N—C), and the peak located at 400.1 eV is attributed to tertiary nitrogen N—$(C)_3$ [40,41]. The two small peaks at 401.3 and 404.2 eV are corresponding to N—H groups and charging effects, respectively [42,43]. In the O 1*s* spectra of the RT and RTCN samples, the peak located at 529.7 eV is originated from bulk Ti—O—Ti bonding [44]. Simultaneously, the peak at 532.1 eV can be assigned to the surface oxygen species including in the adsorbed H_2O or CO_2 and the surface Ti—O—Ti bonding for the CN, RT and RTCN samples [45]. In the Ti 2*p* spectra of the RT and RTCN samples, the two peaks at 458.4 and 464.2 eV can be identified as Ti $2p_{3/2}$ and Ti $2p_{1/2}$ of the Ti^{4+} species, respectively[46,47]. It is worth noting that the locations of peaks associated to the $2p_2$-bonded nitrogen and carbon atoms of the aromatic g-C_3N_4 or the locations of Ti 2*p* of rutile-TiO_2 in the RTCN sample keeps the same as the counterparts of the pure CN and RT samples, suggesting that there is no obvious interfacial electronic interaction between CN and RT in the RTCN sample.

The morphologies of samples were further examined by TEM and HRTEM. As seen from Fig. 7a, the CN sample exhibits a laminar structure, the RT sample shows typical nanoparticles with sizes less than 20 nm, whereas the RT nanoparticles are uniformly dispersed in the CN nanosheets over the RTCN sample. At the same time, Fig. 7d and 7e clearly shows that the lattice spacing of 0.325 nm, which is corresponded to the (1 1 0) crystal plane of rutile TiO_2. In addition, the HRTEM image of the RTCN sample also shows that the clear lattice fringes of RT nanoparticles, intimately couples with the vague fringes of CN nanosheets [48,49]. Thus, the intimate interface contact of CN and RT is a prerequisite for the formation of heterojunction over the RTCN sample, and the further proofs will be given in the latter experimental results.

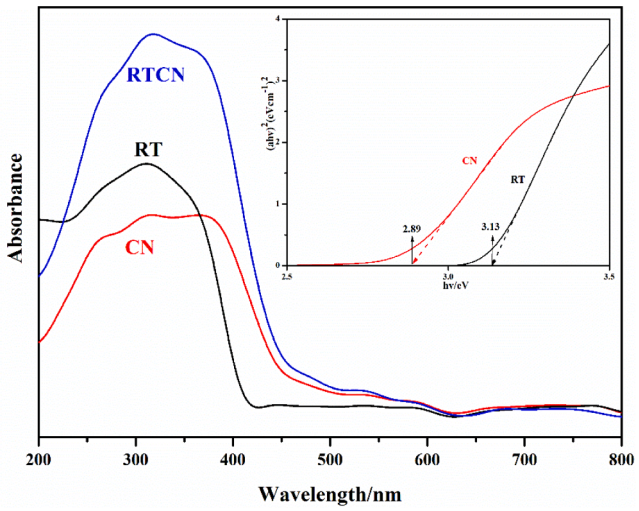

Fig. 8. UV–Vis DRS and Tauc plots of the CN, RT and RTCN samples.

3.3. Optical property

The optical properties of CN, RT and RTCN samples were evaluated by using UV–Vis DRS. As shown in Fig. 8, it can be seen that the fundamental absorption edges of the CN and RT samples are at around 441 nm and 400 nm, respectively. It is found that the RTCN sample exhibits the strongest light absorption, which can be mainly on account of the heterojunction formed between CN and RT [50,51].

The bandgap energies of the as-prepared samples can be calculated by the following formula [52].

$$(\alpha h\nu)^2 = A \times (h\nu - Eg) \quad (1)$$

Where α, h, ν, Eg and A are absorption coefficient, Plank's constant, the light frequency, direct bandgap and a constant, respectively. According to the Tauc plot of $(\alpha h\nu)^2$ versus $h\nu$ (inset of Fig. 8), the Eg values of the CN and RT are estimated to be 2.89 and 3.13 eV, respectively.

EIS was measured to investigate the separation efficiency of photogenerated carriers, as presented in Fig. 9a. Accordingly, a smaller impedance arc radius means a lower charge transfer resistance and a higher charge separation efficiency [53]. As can be seen, the arc radius of the RTCN sample is much smaller than those of the CN and RT samples, and it is deduced that the heterojunction of the RTCN sample can accelerate charge transfer and inhibit charge recombination. In order to further inspect the transfer properties of the photogenerated carriers, the transient photocurrent density of sample was conducted. As shown in Fig. 9b, the intensity of photocurrent density obeys the sequence of RTCN > CN > RT. The RTCN sample possesses the highest photocurrent density of 70nA·cm^{-2}, which is almost 2.8 and 3.5 times higher than that of the CN sample (25nA·cm^{-2}) and the RT sample (20nA·cm^{-2}), respectively. Simultaneously, the results also corroborate that the formation of heterojunction over the RTCN sample is conductive to the separation and migration of photogenerated carriers [54].

Furthermore, the Mott-Schottky plots were measured to characterize the band structures of CN and RT, as shown in Fig. 9c. The positive slope of the two samples is indicative of the characterization of *n*-type semiconductor [55–57]. Generally, the conduction band (CB) potential value of semiconductor is approximately equal to its flat band potential [58]. Therefore, the CB potentials of the CN and RT samples are at −0.93 and 0.05 V (vs normal hydrogen electrode (NHE)), respectively. According to the empirical formula: $E_{VB} = E_{CB} + Eg$, the valence band (VB) potentials of the CN and RT samples are 1.96 and 3.18 V, respectively.

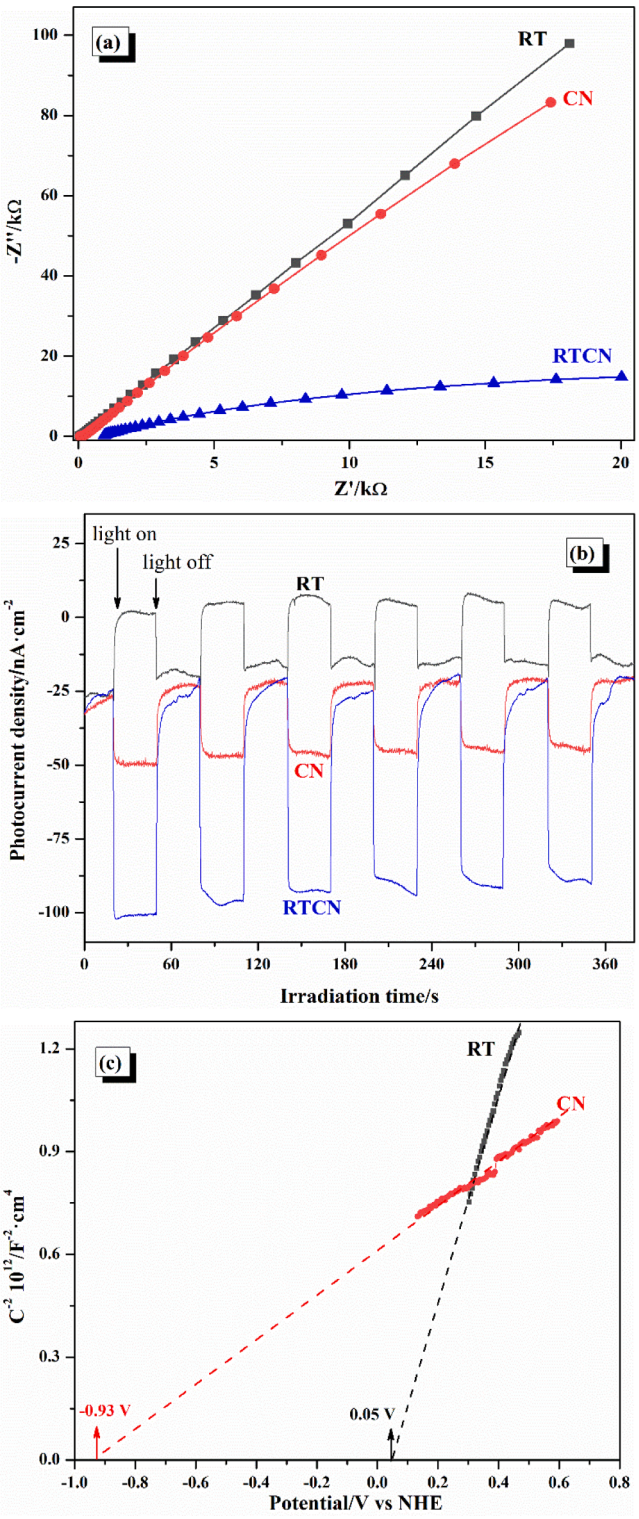

Fig. 9. (a) EIS and (b) the transient photocurrent densities of the CN, RT and RTCN samples, and (c) Mott-Schottky plots of the CN and RT samples.

3.4. Mechanism of photocatalytic reaction

To ascertain the roles of active species during the RhB photodegradation reaction over the photocatalysts, the trapping experiments were carried out through adding different scavengers. EDTA-2Na, p-BQ and IPA were used as the scavengers of holes (h^+), superoxide radicals ($^{\bullet}O_2^-$) and hydroxyl radicals ($^{\bullet}OH$), respectively [59]. As shown in

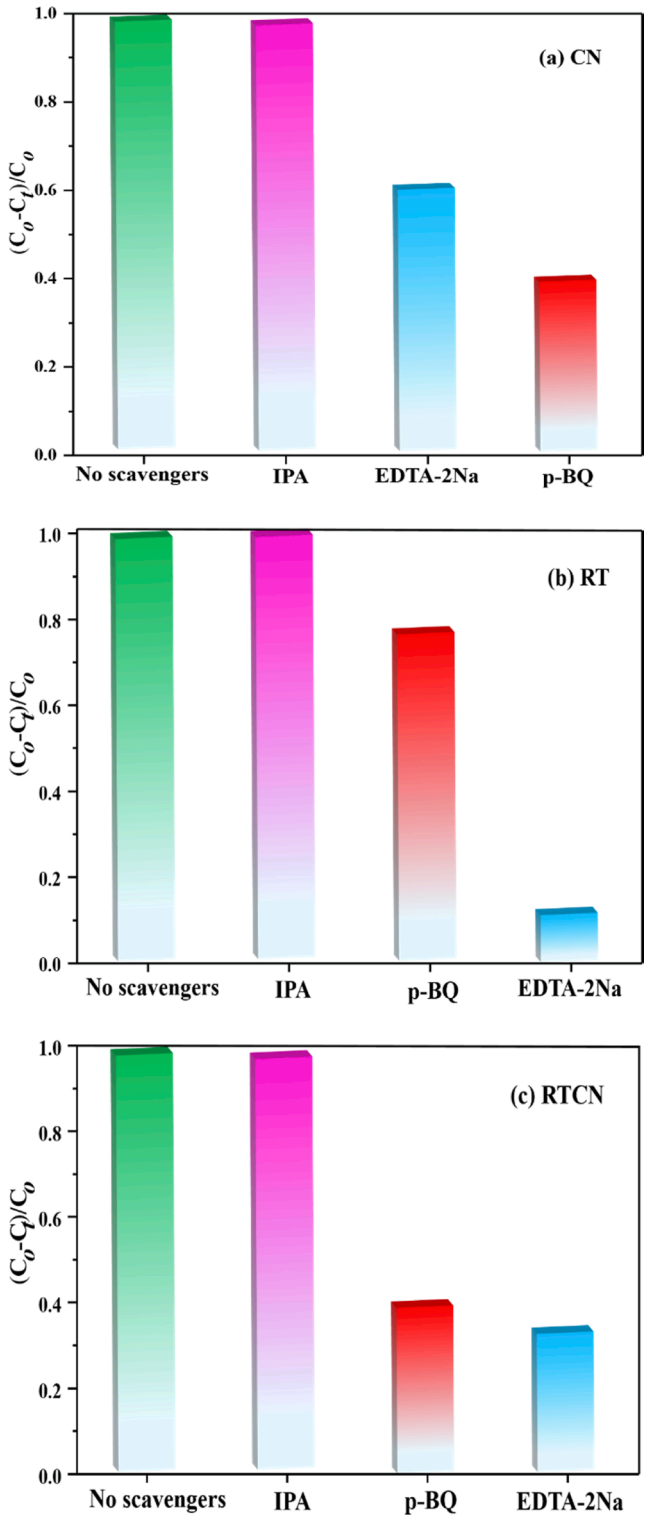

Fig. 10. The photodegradation efficiency of RhB over (a) CN, (b) RT and (c) RTCN in the presence of different scavengers.

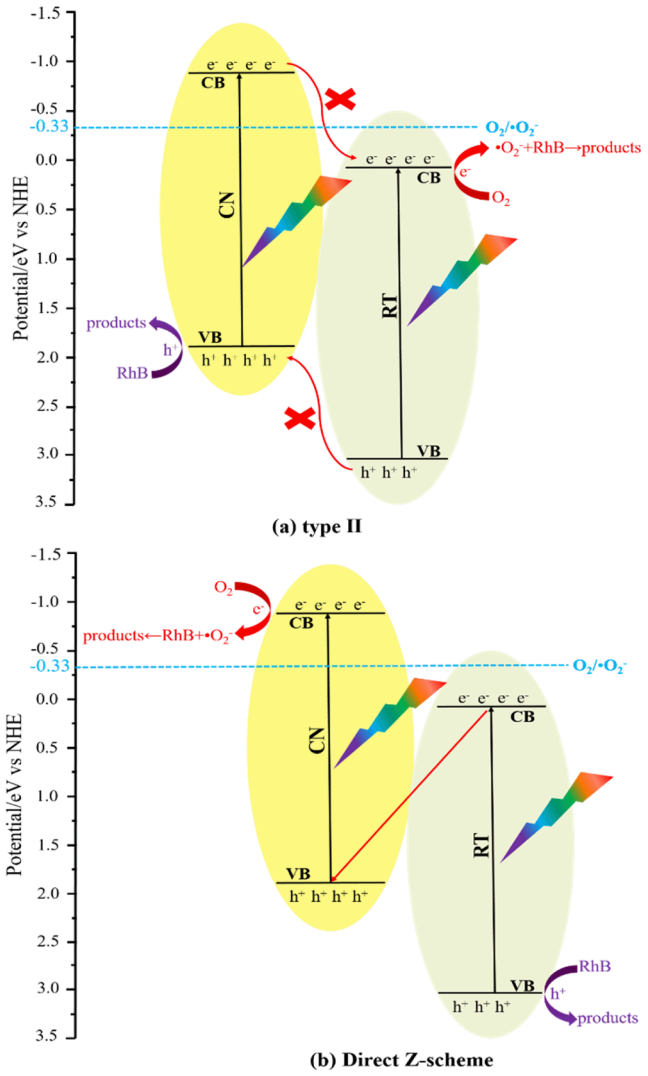

Fig. 11. Schematic illustrations of photocatalytic reaction mechanism over the RTCN photocatalyst: (a) the type-II heterojunction mechanism; (b) the direct Z-scheme heterojunction mechanism.

Fig. 10a, the photocatalytic efficiency of RhB obviously declines after the addition of p-BQ and EDTA-2Na and the order of suppression degree is p-BQ > EDTA-2Na, whereas the effect caused by IPA can be almost ignored. Therefore, it is speculated that $^{\bullet}O_2^-$ is the most important active radical for the CN sample. Accordingly, as observed from Fig. 10b, only EDTA-2Na can significantly inhibit the photocatalytic activity of the RT sample, and the degradation efficiency of RhB follows the order of IPA > p-BQ > EDTA-2Na, which manifests that the photogenerated h^+ is major active species in the photodegradation process over the RT sample. As for the RTCN sample, it can be seen from Fig. 10c that the photocatalytic activity can be severely inhibited by both p-BQ and EDTA-2Na. Consequently, it can be deducted that both the photogenerated h^+ and $^{\bullet}O_2^-$ are the main active species during the RhB photodegradation process over the RTCN sample.

Based on the above discussions, the possible photodegradation mechanism is proposed to explain the enhanced photocatalytic activity of the RTCN sample shown in Fig. 11. Under the simulated sunlight irradiation, electrons are excited to CB and holes are formed in VB of semiconductor photocatalysts, and the photogenerated carriers readily migrate at the interface of photocatalysts to react with reactants [60]. As illustrated in Fig. 11a, the positions of the CB and VB edges of the CN sample are higher than that of the RT sample. According to the type-II heterojunction theory, the photogenerated e^- in the CB of CN will transfer to the CB of RT and the photogenerated h^+ in the VB of RT will migrate to the VB of CN [61]. However, the photogenerated e^- in CB of RT cannot react with the dissolved O_2 near the surface of the catalyst to generate $^{\bullet}O_2^-$ radicals because the E_{CB} of RT is more positive than the standard redox potential of $O_2/^{\bullet}O_2^-$ (-0.33 eV) [62]. In this sense, the type-II heterojunction mechanism conflicts with the results of trapping experiment in which $^{\bullet}O_2^-$ is the main reactive species over the RTCN sample. To this end, the direct Z-scheme heterojunction mechanism is

proposed to explain the elevated photocatalytic performance of RTCN system, as presented in Fig. 11b. The photogenerated e^- in the CB of RT can directly transfer to the VB of CN through the contact interface and recombine with the holes in the VB of CN. Moreover, the photogenerated e^- in the CB of CN (-0.93 eV) can react with O_2 to form $\cdot O_2^-$ and $\cdot O_2^-$ further oxidizes RhB. Meanwhile, the photogenerated h^+ in the VB of RT can also directly oxidize RhB. It can be seen that the direct Z-scheme heterojunction mechanism can reasonably explain the results of trapping experiment over the RTCN photocatalyst. Therefore, this allows one to conclude that the direct Z-scheme heterojunction rutile-TiO_2/g-C_3N_4 photocatalyst is constructed by solid grinding method to improve its photocatalytic performance.

4. Conclusion

In summary, the rutile-TiO_2/g-C_3N_4 photocatalyst with direct Z-scheme heterojunction can be successfully synthesized by a facile solid grinding method without any other treatment. The rutile-TiO_2/g-C_3N_4 photocatalyst composites with 2:5 mass ratio of rutile-TiO_2 to g-C_3N_4 exhibits the best photocatalytic performance, which can be mainly ascribed to the enhanced ability of light absorption and the higher separation efficiency of photogenerated carriers. The results of trapping experiments and the analysis results of band structure by UV–Vis DRS and electrochemical measurements confirm the direct Z-scheme heterojunction mechanism over the rutile-TiO_2/g-C_3N_4 photocatalyst.

CRediT authorship contribution statement

Genxiang Li: Methodology, Data curation, Investigation, Writing – original draft. **Yandi Cai:** Methodology, Data curation. **Xiudie Wang:** Methodology, Formal analysis. **Lei Zhang:** Conceptualization, Writing – review & editing, Project administration, Resources, Funding acquisition. **Qiao Xie:** Software, Supervision. **Peng Chen:** Formal analysis. **Chuanjiang Li:** Supervision. **Jingfang Sun:** Project administration, Resources. **Tingzhen Li:** Supervision, Project administration, Resources. **Lin Dong:** Resources.

Declaration of Competing Interest

The authors declare that they have no known competing financial interests or personal relationships that could have appeared to influence the work reported in this paper.

Acknowledgements

This work is financially supported by the National Natural Science Foundation of China (No. 21607019), the Scientific and Technological Research Program of Chongqing Municipal Education Commission (Nos. KJQN202101242 and KJQN202001227), the Open Project Program of Key Laboratory of Water Environment Evolution and Pollution Control in the Three Gorges Reservoir (No. WEPKL2019ZD-04).

Appendix A. Supplementary material

Supplementary data to this article can be found online at https://doi.org/10.1016/j.chemphys.2022.111558.

References

[1] S. Wang, J.H. Yun, B. Luo, T. Butburee, P. Peerakiatkhajohn, S. Thaweesak, M. Xiao, L. Wang, Recent progress on visible light responsive heterojunctions for photocatalytic applications, J. Mater. Sci. Technol. 33 (2017) 1–22, https://doi.org/10.1016/j.jmst.2016.11.017.
[2] X. Li, J. Yu, M. Jaroniec, Hierarchical photocatalysts, Chem. Soc. Rev. 45 (2016) 2603–2636, https://doi.org/10.1039/c5cs00838g.
[3] Y. Wang, W. Yang, X. Chen, J. Wang, Y. Zhu, Photocatalytic activity enhancement of core-shell structure g-C_3N_4@TiO_2 via controlled ultrathin g-C_3N_4 layer, Appl. Catal. B Environ. 220 (2018) 337–347, https://doi.org/10.1016/j.apcatb.2017.08.004.
[4] J. Lei, Y. Chen, F. Shen, L. Wang, Y. Liu, J. Zhang, Surface modification of TiO_2 with g-C_3N_4 for enhanced UV and visible photocatalytic activity, J. Alloy. Compd. 631 (2015) 328–334, https://doi.org/10.1016/j.jallcom.2015.01.080.
[5] J. Li, M. Zhang, Q. Li, J. Yang, Enhanced visible light activity on direct contact Z-scheme g-C_3N_4-TiO_2 photocatalyst, Appl. Surf. Sci. 391 (2017) 184–193, https://doi.org/10.1016/j.apsusc.2016.06.145.
[6] W.K. Jo, T.S. Natarajan, Influence of TiO_2 morphology on the photocatalytic efficiency of direct Z-scheme g-C_3N_4/TiO_2 photocatalysts for isoniazid degradation, Chem. Eng. J. 281 (2015) 549–565, https://doi.org/10.1016/j.cej.2015.06.120.
[7] J. Li, M. Zhang, X. Li, Q. Li, J. Yang, Effect of the calcination temperature on the visible light photocatalytic activity of direct contact Z-scheme g-C_3N_4-TiO_2 heterojunction, Appl. Catal. B Environ. 212 (2017) 106–114, https://doi.org/10.1016/j.apcatb.2017.04.061.
[8] Z.A. Huang, Q. Sun, K. Lv, Z. Zhang, M. Li, B. Li, Effect of contact interface between TiO_2 and g-C_3N_4 on the photoreactivity of g-C_3N_4/TiO_2 photocatalyst: (001) vs (101) facets of TiO_2, Appl. Catal. B Environ. 164 (2015) 420–427, https://doi.org/10.1016/j.apcatb.2014.09.043.
[9] H. Tang, Q. Shang, Y. Tang, X. Yi, Y. Wei, K. Yin, M. Liu, C. Liu, Static and continuous flow photoelectrocatalytic treatment of antibiotic wastewater over mesh of TiO_2 nanotubes implanted with g-C_3N_4 nanosheets, J. Hazard. Mater. 384 (2020), 121248, https://doi.org/10.1016/j.jhazmat.2019.121248.
[10] G. Jiang, K. Geng, Y. Wu, Y. Han, X. Shen, High photocatalytic performance of ruthenium complexes sensitizing g-C_3N_4/TiO_2 hybrid in visible light irradiation, Appl. Catal. B: Environ. 227 (2018) 366–375, https://doi.org/10.1016/j.apcatb.2018.01.034.
[11] J. Lei, B. Chen, W. Lv, L. Zhou, L. Wang, Y. Liu, J. Zhang, An inverse opal TiO_2/g-C_3N_4 composite with a heterojunction for enhanced visible light-driven photocatalytic activity, Dalton. T. 48 (2019) 3486–3495, https://doi.org/10.1039/C8DT04496A.
[12] J.C. Wang, C.X. Cui, Y. Li, L. Liu, Y.P. Zhang, W. Shi, Porous Mn doped g-C_3N_4 photocatalysts for enhanced synergetic degradation under visible-light illumination, J. Hazard. Mater. 339 (2017) 43–53, https://doi.org/10.1016/j.jhazmat.2017.06.011.
[13] M. Arumugam, M. Tahir, P. Praserthdam, Effect of nonmetals (B, O, P, and S) doped with porous g-C_3N_4 for improved electron transfer towards photocatalytic CO_2 reduction with water into CH_4, Chemosphere 286 (2022), 131765, https://doi.org/10.1016/j.chemosphere.2021.131765.
[14] I. Troppová, M. Šihor, M. Reli, M. Ritz, P. Praus, K. Kočí, Unconventionally prepared TiO_2/g-C_3N_4 photocatalysts for photocatalytic decomposition of nitrous oxide, Appl. Surf. Sci. 430 (2018) 335–347, https://doi.org/10.1016/j.apsusc.2017.06.299.
[15] K. Qi, B. Cheng, J. Yu, W. Ho, A review on TiO_2-based Z-scheme photocatalysts, Chin. J. Catal. 38 (2017) 1936–1955, https://doi.org/10.1016/S1872-2067(17)62962-0.
[16] J. Low, J. Yu, M. Jaroniec, S. Wageh, A.A. Al-Ghamdi, Heterojunction photocatalysts, Adv. Mater. 29 (20) (2017) 1601694.
[17] Y. Li, M. Zhou, B. Cheng, Y. Shao, Recent advances in g-C_3N_4-based heterojunction photocatalysts, J. Mater. Sci. Technol. 56 (2020) 1–17, https://doi.org/10.1016/j.jmst.2020.04.028.
[18] A. Hassani, S. Krishnan, J. Scaria, P. Eghbali, P.V. Nidheesh, Z-scheme photocatalysts for visible-light-driven pollutants degradation: A review on recent advancements, Curr. Opin. Solid. State. Mater. Sci. 25 (5) (2021) 100941.
[19] D. Huang, X. Yan, M. Yan, G. Zeng, C. Zhou, J. Wan, M. Cheng, W. Xue, Graphitic carbon nitride-based heterojunction photoactive nanocomposites: applications and mechanism insight, ACS. Appl. Mater. Inter. 10 (2018) 21035–21055, https://doi.org/10.1021/acsami.8b03620.
[20] Y. Li, M. Gu, X. Zhang, J. Fan, K. Lv, S. Carabineiro, F. Dong, 2D g-C_3N_4 for advancement of photo-generated carrier dynamics: status and challenges, Mater. Today 41 (2020) 270–303, https://doi.org/10.1016/j.mattod.2020.09.004.
[21] J. Hao, S. Zhang, F. Ren, Z. Wang, J. Lei, X. Wang, T. Cheng, L. Li, Synthesis of TiO_2@g-C_3N_4 core-shell nanorod arrays with Z-scheme enhanced photocatalytic activity under visible light, J. Colloid. Interf. Sci. 508 (2017) 419–425, https://doi.org/10.1016/j.jcis.2017.08.065.
[22] Y. Xia, L. Xu, J. Peng, J. Han, S. Guo, L. Zhang, Z. Han, S. Komarneni, TiO_2@g-C_3N_4 core/shell spheres with uniform mesoporous structures for high performance visible-light photocatalytic application, Ceram. Int. 45 (2019) 18844–18851, https://doi.org/10.1016/j.ceramint.2019.06.118.
[23] Y. Li, K. Lv, W. Ho, F. Dong, X. Wu, Y. Xia, Hybridization of rutile TiO_2(rTiO_2) with g-C_3N_4 quantum dots (CN QDs): An efficient visible-light-driven Z-scheme hybridized photocatalyst, Appl. Catal. B: Environ. 202 (2017) 611–619, https://doi.org/10.1016/j.apcatb.2016.09.055.
[24] Y. Sheng, Z. Wei, H. Miao, W. Yao, H. Li, Y. Zhu, Enhanced organic pollutant photodegradation via adsorption/photocatalysis synergy using a 3D g-C_3N_4/TiO_2 free-separation photocatalyst, Chem. Eng. J. 370 (2019) 287–294, https://doi.org/10.1016/j.cej.2019.03.197.
[25] J. Wang, G. Wang, B. Cheng, J. Yu, J. Fan, Sulfur-doped g-C_3N_4/TiO_2 S-scheme heterojunction photocatalyst for Congo Red photodegradation, Chin. J. Catal. 42 (2021) 56–68, https://doi.org/10.1016/S1872-2067(20)63634-8.
[26] P. Li, X. Zhang, L. Qiu, X. Xu, Y. Si, T. Liang, H. Liu, J. Chu, J. Guo, S. Duo, MOF-derived TiO_2 modified with g-C_3N_4 nanosheets for enhanced visible-light photocatalytic performance, New. J. Chem. 44 (2020) 6958–6964, https://doi.org/10.1039/d0nj00746c.

[27] T. Watanabe, T. Takirawa, K. Honda, Photocatalysis through excitation of adsorbates. 1. Highly efficient N-deethylation of Rhodamine B adsorbed to CdS, J. Phys. Chem. 81 (1977) 1845–1851, https://doi.org/10.1021/j100534a012.
[28] T. Takirawa, T. Watanabe, K. Honda, Photocatalysis through excitation of adsorbates. 2. A comparative study of rhodamine B and methylene blue on cadmium sulfide, J. Phys. Chem. 82 (1978) 1391–1396, https://doi.org/10.1021/j100501a014.
[29] J. Zhuang, W. Dai, Q. Tian, Z. Li, L. Xie, J. Wang, P. Liu, X. Shi, D. Wang, Photocatalytic degradation of RhB over TiO_2 bilayer films: effect of defects and their location, Langmuir 26 (2010) 9686–9694, https://doi.org/10.1021/la100302m.
[30] C. Yao, X. Wang, W. Zhao, T. Li, Y. He, X. Ran, L. Guo, Probing the facet-dependent intermediate in the visible-light degradation of RhB by carbon-coated anatase TiO_2 nanoparticles, J. Alloy. Compd. 846 (2020), 156335, https://doi.org/10.1016/j.jallcom.2020.156335.
[31] X. Chen, J. Wei, R. Hou, Y. Liang, Z. Xie, Y. Zhu, X. Zhang, H. Wang, Growth of g-C_3N_4 on mesoporous TiO_2 spheres with high photocatalytic activity under visible light irradiation, Appl. Catal. B: Environ. 188 (2016) 342–350, https://doi.org/10.1016/j.apcatb.2016.02.012.
[32] X. Wang, F. Wang, C. Bo, K. Cheng, J. Wang, J. Zhang, H. Song, Promotion of phenol photodecomposition and the corresponding decomposition mechanism over g-C_3N_4/TiO_2 nanocomposites, Appl. Surf. Sci. 453 (2018) 320–329, https://doi.org/10.1016/j.apsusc.2018.05.082.
[33] Y. Zhang, S.M. Zhao, Q.-W. Su, J.L. Xu, Visible light response ZnO-C_3N_4 thin film photocatalyst, Rare Metals 40 (2019) 96–104, https://doi.org/10.1007/s12598-019-01297-0.
[34] R. Hao, G. Wang, H. Tang, L. Sun, C. Xu, D. Han, Template-free preparation of macro/mesoporous g-C_3N_4/TiO_2 heterojunction photocatalysts with enhanced visible light photocatalytic activity, Appl. Catal. B: Environ. 187 (2016) 47–58, https://doi.org/10.1016/j.apcatb.2016.01.026.
[35] R. Hao, G. Wang, C. Jiang, H. Tang, Q. Xu, In situ hydrothermal synthesis of g-C_3N_4/TiO_2 heterojunction photocatalysts with high specific surface area for Rhodamine B degradation, Appl. Surf. Sci. 411 (2017) 400–410, https://doi.org/10.1016/j.apsusc.2017.03.197.
[36] O. Elbanna, M. Fujitsuka, T. Majima, g-C_3N_4/TiO_2 mesocrystals composite for H_2 evolution under visible-light irradiation and its charge carrier dynamics, ACS Appl. Mater. Inter. 9 (2017) 34844–34854, https://doi.org/10.1021/acsami.7b08548.
[37] J. Wang, G. Wang, X. Wang, Y. Wu, Y. Su, H. Tang, 3D/2D direct Z-scheme heterojunctions of hierarchical TiO_2 microflowers/g-C_3N_4 nanosheets with enhanced charge carrier separation for photocatalytic H_2 evolution, Carbon 149 (2019) 618–626, https://doi.org/10.1016/j.carbon.2019.04.088.
[38] W.W. Liu, J. Pan, R.F. Peng, Shape-dependent hydrogen generation performance of PtPd bimetallic co-catalyst coupled with C_3N_4 photocatalyst, Rare Metals 40 (2021) 3554–3560, https://doi.org/10.1007/s12598-021-01705-4.
[39] T. Giannakopoulou, I. Papailias, N. Todorova, N. Boukos, Y. Liu, J. Yu, C. Trapalis, Tailoring the energy band gap and edges' potentials of g-C_3N_4/TiO_2 composite photocatalysts for NOx removal, Chem. Eng. J. 310 (2017) 571–580, https://doi.org/10.1016/j.cej.2015.12.102.
[40] C. Sun, H. Zhang, H. Liu, X. Zheng, W. Zou, L. Dong, L. Qi, Enhanced activity of visible-light photocatalytic H_2 evolution of sulfur-doped g-C_3N_4 photocatalyst via nanoparticle metal Ni as cocatalyst, Appl. Catal. B: Environ. 235 (2018) 66–74, https://doi.org/10.1016/j.apcatb.2018.04.050.
[41] H. Wang, Y. Liang, L. Liu, J. Hu, W. Cui, Highly ordered TiO_2 nanotube arrays wrapped with g-C_3N_4 nanoparticles for efficient charge separation and increased photoelectrocatalytic degradation of phenol, J. Hazard. Mater. 344 (2018) 369–380, https://doi.org/10.1016/j.jhazmat.2017.10.044.
[42] X. Du, X. Bai, L. Xu, L. Yang, P. Jin, Visible-light activation of persulfate by TiO_2/g-C_3N_4 photocatalyst toward efficient degradation of micropollutants, Chem. Eng. J. 384 (2020), 123245, https://doi.org/10.1016/j.cej.2019.123245.
[43] X. Song, Y. Hu, M. Zheng, C. Wei, Solvent-free in situ synthesis of g-C_3N_4/{001} TiO_2 composite with enhanced UV- and visible-light photocatalytic activity for NO oxidation, Appl. Catal. B: Environ. 182 (2016) 587–597, https://doi.org/10.1016/j.apcatb.2015.10.007.
[44] W. Wang, J. Fang, S. Shao, M. Lai, C. Lu, Compact and uniform TiO_2@g-C_3N_4 core-shell quantum heterojunction for photocatalytic degradation of tetracycline antibiotics, Appl. Catal. B: Environ. 217 (2017) 57–64, https://doi.org/10.1016/j.apcatb.2017.05.037.
[45] P. Lv, C. Zhao, W.J. Lee, S. Huo, S.H. Kwon, J. Fang, Y. Yang, Less is more: Enhancement of photocatalytic activity of g-C_3N_4 nanosheets by site-selective atomic layer deposition of TiO_2, Appl. Surf. Sci. 494 (2019) 508–518, https://doi.org/10.1016/j.apsusc.2019.07.131.
[46] W. Tao, M. Wang, R. Ali, S. Nie, Q. Zeng, R. Yang, W.-M. Lau, L. He, H. Tang, X. Jian, Multi-layered porous hierarchical TiO_2/g-C_3N_4 hybrid coating for enhanced visible light photocatalysis, Appl. Surf. Sci. 495 (2019), 143435, https://doi.org/10.1016/j.apsusc.2019.07.131.
[47] T. Tang, L. You, P. Liang, T. Jia, W. Feng, Q. Liu, F. Li, W. Zhu, D. Wang, J. Wu, Tuning dimensionality TiO_2/g-C_3N_4 heterostructure for enhanced elemental mercury removal performance under visible-light, Chem. Phys. Lett. 782 (2021), 139027, https://doi.org/10.1016/j.cplett.2021.139027.
[48] Y. Tan, Z. Shu, J. Zhou, T. Li, W. Wang, Z. Zhao, One-step synthesis of nanostructured g-C_3N_4/TiO_2 composite for highly enhanced visible-light photocatalytic H_2 evolution, Appl. Catal. B: Environ. 230 (2018) 260–268, https://doi.org/10.1016/j.apcatb.2018.02.056.
[49] Z. Wei, F. Liang, Y. Liu, W. Luo, J. Wang, W. Yao, Y. Zhu, Photoelectrocatalytic degradation of phenol-containing wastewater by TiO_2/g-C_3N_4 hybrid heterostructure thin film, Appl. Catal. B: Environ. 201 (2017) 600–606, https://doi.org/10.1016/j.apcatb.2016.09.003.
[50] J. Yan, H. Wu, H. Chen, Y. Zhang, F. Zhang, S.F. Liu, Fabrication of TiO_2/C_3N_4 heterostructure for enhanced photocatalytic Z-scheme overall water splitting, Appl. Catal. B: Environ. 191 (2016) 130–137, https://doi.org/10.1016/j.apcatb.2016.03.026.
[51] Q. Wang, L. Zhang, Y. Guo, M. Shen, M. Wang, B. Li, J. Shi, Multifunctional 2D porous g-C_3N_4 nanosheets hybridized with 3D hierarchical TiO_2 microflowers for selective dye adsorption, antibiotic degradation and CO_2 reduction, Chem. Eng. J. 396 (2020), 125347, https://doi.org/10.1016/j.cej.2020.125347.
[52] Q. Tang, X. Meng, Z. Wang, J. Zhou, H. Tang, One-step electrospinning synthesis of TiO_2/g-C_3N_4 nanofibers with enhanced photocatalytic properties, Appl. Surf. Sci. 430 (2018) 253–262, https://doi.org/10.1016/j.apsusc.2017.07.288.
[53] X. Wei, X. Wang, Y. Pu, A. Liu, C. Chen, W. Zou, Y. Zheng, J. Huang, Y. Zhang, Y. Yang, M. Naushad, B. Gao, L. Dong, Facile ball-milling synthesis of CeO_2/g-C_3N_4 Z-scheme heterojunction for synergistic adsorption and photodegradation of methylene blue: Characteristics, kinetics, models, and mechanisms, Chem. Eng. J. 420 (2021), 127719, https://doi.org/10.1016/j.cej.2020.127719.
[54] W. Wu, X. Li, Z. Ruan, Y. Li, X. Xu, Y. Yuan, K. Lin, Fabrication of a TiO_2 trapped meso/macroporous g-C_3N_4 heterojunction photocatalyst and understanding its enhanced photocatalytic activity based on optical simulation analysis, Inorg. Chem. Front. 5 (2018) 481–489, https://doi.org/10.1039/x0xx00000x.
[55] W. Gu, F. Lu, C. Wang, S. Kuga, L. Wu, Y. Huang, M. Wu, Face-to-face interfacial assembly of ultrathin g-C_3N_4 and anatase TiO_2 nanosheets for enhanced solar photocatalytic activity, ACS Appl. Mater. Inter. 9 (2017) 28674–28684, https://doi.org/10.1021/acsami.7b10010.
[56] C. Yang, J. Qin, Z. Xue, M. Ma, X. Zhang, R. Liu, Rational design of carbon-doped TiO_2 modified g-C_3N_4 via in-situ heat treatment for drastically improved photocatalytic hydrogen with excellent photostability, Nano Energy 41 (2017) 1–9, https://doi.org/10.1016/j.nanoen.2017.09.012.
[57] F. He, B. Zhu, B. Cheng, J. Yu, W. Ho, W. Macyk, 2D/2D/0D TiO_2/C_3N_4/Ti_3C_2 MXene composite S-scheme photocatalyst with enhanced CO_2 reduction activity, Appl. Catal. B: Environ. 272 (2020), 119006, https://doi.org/10.1016/j.apcatb.2020.119006.
[58] T. Jiang, K. Wang, T. Guo, X. Wu, G. Zhang, Fabrication of Z-scheme MoO_3/Bi_2O_4 heterojunction photocatalyst with enhanced photocatalytic performance under visible light irradiation, Chin. J. Catal 41 (2020) 161–169, https://doi.org/10.1016/S1872-2067(19)63391-7.
[59] N. Guo, Y. Zeng, H. Li, X. Xu, H. Yu, X. Han, Novel mesoporous TiO_2@g-C_3N_4 hollow core@shell heterojunction with enhanced photocatalytic activity for water treatment and H_2 production under simulated sunlight, J. Hazard. Mater. 353 (2018) 80–88, https://doi.org/10.1016/j.jhazmat.2018.03.044.
[60] S.T. Huang, J.B. Zhong, J.Z. Li, J.F. Chen, Z. Xiang, W. Hu, M. Li, Z-scheme TiO_2/g-C_3N_4 composites with improved solar-driven photocatalytic performance deriving from remarkably efficient separation of photo-generated charge pairs, Mater. Res. Bull. 84 (2016) 65–70, https://doi.org/10.1016/j.materresbull.2016.07.036.
[61] D. Zhou, B. Yu, Q. Chen, H. Shi, Y. Zhang, D. Li, X. Yang, W. Zhao, C. Liu, G. Wei, Z. Chen, Improved visible light photocatalytic activity on Z-scheme g-C_3N_4 decorated TiO_2 nanotube arrays by a simple impregnation method, Mater. Res. Bull. 124 (2020), 110757, https://doi.org/10.1016/j.materresbull.2019.110757.
[62] X. Ma, Q. Chen, G. Liu, Y. Zhou, D. Maa, S. Xin, C. Yu, B. Zhang, Y. Xin, Construction of netlike 3D Z-scheme photoelectrodes with improved photocatalytic performance based on g-C_3N_4 nanosheets modified TiO_2 nanobelt-tubes, Chem. Eng. Sci. 226 (2020), 115844, https://doi.org/10.1016/j.ces.2020.115844.